Geophysical Research Letters

RESEARCH LETTER

10.1029/2021GL092756

Key Points:

- First satellite observations of atmospheric gravity waves using Aeolus
- A case study is presented of an orographic gravity wave over the Southern Andes with coherent phase structure down to the surface
- Results reproduce well in satellite observations and reanalysis data

Correspondence to:

T. P. Banyard,
tpb38@bath.ac.uk

Citation:

Banyard, T. P., Wright, C. J., Hindley, N. P., Halloran, G., Krisch, I., Kaifler, B., & Hoffmann, L. (2021). Atmospheric gravity waves in Aeolus wind lidar observations. *Geophysical Research Letters*, *48*, e2021GL092756. https://doi.org/10.1029/2021GL092756

Received 19 FEB 2021
Accepted 22 APR 2021

Author Contributions:

Conceptualization: T. P. Banyard, C. J. Wright, N. P. Hindley, G. Halloran, I. Krisch
Data curation: T. P. Banyard, B. Kaifler, L. Hoffmann
Formal analysis: T. P. Banyard
Funding acquisition: C. J. Wright
Investigation: T. P. Banyard
Methodology: T. P. Banyard, C. J. Wright, N. P. Hindley, G. Halloran, I. Krisch
Project Administration: T. P. Banyard, C. J. Wright
Resources: T. P. Banyard, C. J. Wright, B. Kaifler, L. Hoffmann
Software: T. P. Banyard
Supervision: C. J. Wright, N. P. Hindley
Validation: T. P. Banyard
Visualization: T. P. Banyard
Writing – original draft: T. P. Banyard, C. J. Wright, N. P. Hindley

Atmospheric Gravity Waves in Aeolus Wind Lidar Observations

T. P. Banyard[1], C. J. Wright[1], N. P. Hindley[1], G. Halloran[2], I. Krisch[3], B. Kaifler[3], and L. Hoffmann[4]

[1]Centre for Space, Atmospheric and Oceanic Science, University of Bath, Bath, UK, [2]Met Office, Exeter, UK, [3]DLR, Institut für Physik der Atmosphäre, Oberpfaffenhofen, Germany, [4]Jülich Supercomputing Centre, Forschungszentrum Jülich, Jülich, Germany

Abstract Aeolus is the first Doppler wind lidar in space. It provides unique high-resolution measurements of horizontal wind in the sparsely observed upper-troposphere/lower-stratosphere (UTLS), with global coverage. In this study, Aeolus' ability to resolve atmospheric gravity waves (GWs) is demonstrated. The accurate representation of these small-scale waves is vital to properly simulate dynamics in global weather and climate models. In a case study over the Andes, Aeolus GW measurements show coherent phase structure from the surface to the lower stratosphere, with wind perturbations >10 ms^{-1}, a vertical wavelength $\sim$8 km, and an along-track horizontal wavelength $\sim$900 km. Good agreement is found between Aeolus and co-located satellite, ground-based lidar and reanalysis data sets for this example. Our results show that data from satellites of this type can provide unique information on GW sources and propagation in the UTLS, filling a key knowledge gap that underlies known major deficiencies in weather and climate modeling.

Plain Language Summary Gravity waves are an important driver of the global atmospheric circulation, but are difficult to observe due to their scale size and location. Existing satellite observations reveal these waves in temperature perturbations, but tend to be limited in either vertical or horizontal resolution. Since they are, arguably, best described in a wind-based mathematical framework, and due to their influential behavior in the upper-troposphere lower-stratosphere region, an observing platform that satisfies both of these requirements could prove very significant. This study explores the capability of the first Doppler wind lidar in space, Aeolus, to measure gravity waves and provide unique information about their sources and propagation through the atmosphere. Significantly, Aeolus measures wind speed directly and is well suited to observe the upper-troposphere lower-stratosphere region. Here, a case study is presented showing observations of a strong gravity wave produced by the enhanced orography of the Southern Andes, which are the most prominent hotspot of gravity wave activity globally. Results are validated against two other observational instruments and atmospheric reanalysis, and give confidence in Aeolus' ability to measure these phenomena.

1. Introduction

Atmospheric gravity waves (GWs) are small-scale propagating disturbances that arise due to the vertical forcing of air parcels by a disturbance in the flow. They are generated by a variety of meteorological processes, including flow over orography, atmospheric deep convection, and jet stream, cyclonic, and frontal instabilities. GWs play a wide range of key roles in the atmospheric system, particularly in the transfer of energy and momentum (e.g., Fritts & Alexander, 2003). They are responsible for driving the large-scale circulation in the middle atmosphere, primarily through accelerations to the mean-flow by the convergence of GW momentum flux (Fritts, 1984). They also modulate phenomena such as the Quasi-Biennial Oscillation (Dunkerton, 1997; Ern et al., 2014), affect stratosphere-mesosphere coupling during Sudden Stratospheric Warmings (Siskind et al., 2007; Wright et al., 2010), and can produce turbulence when they dissipate that is dangerous to aircraft (Bramberger et al., 2018; Lilly, 1978).

Both climate and numerical weather prediction (NWP) models rely on accurately representing the propagation of GWs from sources near the surface to the upper-troposphere/lower-stratosphere (UTLS) region. This accuracy is needed to correctly simulate important features of the atmosphere, such as the strength of the

Writing – review & editing: T. P. Banyard, C. J. Wright, N. P. Hindley, G. Halloran, I. Krisch, B. Kaifler, L. Hoffmann

northern and southern hemispheric jet streams (Alexander et al., 2010; Ehard et al., 2017; Holton, 1983; McFarlane, 1987; Sato et al., 2012). As such, a limited understanding of the drag forces GWs exert on the mean winds has historically proven to be a significant barrier to advances in NWP, and improvements in GW simulation have often led to model-wide improvements across a range of processes and scales (Eichinger et al., 2020; Palmer et al., 1986). As model resolutions continue to improve, particularly in the vertical dimension, capturing GW processes is becoming an increasingly important problem, and this trend is likely to continue in the near future (Jones et al., 1997; Kim et al., 2003; Watanabe et al., 2015).

Most GWs are currently parametrized in general circulation models (GCMs) (Alexander & Barnet, 2007; Geller et al., 2013). However, in practice these parametrizations are not well constrained observationally due to both the relatively small spatial scales of most GWs and because the GW field varies dramatically across a large range of spatiotemporal frequencies (Alexander, 1998; Alexander et al., 2010). This has long been identified as an important knowledge gap, and since the first empirical measurements of GWs (Hines, 1960), observations have been made using a wide variety of methods.

In-situ observations such as those from radiosondes, aircraft, and meteorological rockets often form an anchor point against which other measurements can be validated (Krisch et al., 2017; B. Sun et al., 2010). Satellite-based observations of GWs are provided by nadir-sounders such as the Atmospheric Infrared Sounder (AIRS) and AMSU, as well as limb-sounders such as the HIRDLS and the COSMIC GPS constellation. These instruments typically measure infra-red radiances from which wind perturbations must be inferred using a set of GW dispersion relations (Ern et al., 2004; Hindley et al., 2015; Wright, Hindley, & Mitchell, 2016; Wright, Hindley, Moss, & Mitchell, 2016). Finally, there are ground-based radars and lidars which provide good temporal coverage at a reasonable vertical resolution (N. Kaifler et al., 2020). These, however, are fixed to one location and cannot provide a global climatology of GW activity by themselves.

Radars and lidars, in particular, provide direct measurements of the wind perturbations induced by GWs (e.g., Larsen et al., 1982; Vincent & Reid, 1983) which is important because GWs are arguably best-described, at a theoretical level, in a wind-based mathematical framework. However, the existing inability to systematically measure winds from space means that relatively few GW measurements have been made using wind perturbations directly other than at these radar and lidar sites, and none to date on a global domain. In 2018, however, the first spaceborne wind lidar instrument was launched aboard the European Space Agency's Aeolus mission. This novel ability to systematically measure winds from space offers the potential to significantly advance the current understanding of how GWs propagate in the real atmosphere, and in turn, to advance weather and climate modeling. As an example, the assimilation of infra-red radiances from existing satellite measurements can now be combined with wind information from Aeolus to potentially further constrain GW momentum fluxes, which are key to model parametrization schemes. Despite observing only a single wind component, the satellite's fine vertical resolution and high laser pulse frequency opens up the possibility for simultaneously measuring both the horizontal and vertical wavelengths of GWs, shown by Ern et al. (2004) to be key in calculating GW momentum fluxes.

To demonstrate the benefits of using Aeolus and its proposed successors as a platform for systematic GW observations, presented here is a case study using Aeolus data to examine the structure of a large GW observed in winter (July) 2019 over the Andes mountains. The Andes are a fantastic natural laboratory for observing GWs due to the ridge at their southern end which is transverse to the prevailing westerly winds. Globally, the Andes are by far the most prominent hotspot of GW activity, and the strong orographic forcing often present can produce waves of large magnitude which propagate to significant distances into the middle and upper atmosphere (Alexander & Teitelbaum, 2011; Hoffmann et al., 2013; Jiang et al., 2002). Additionally, Aeolus' high inclination orbit is oriented approximately parallel to the southern Andean ridge line, measuring a horizontal line-of-sight (HLOS) wind that is close to zonal, and approximately transverse to the mountains at this latitude. Detection conditions here are, therefore, well-suited for a study of this type, which will be generalized to more complicated cases at the global scale in future work.

Section 2 describes the data sources and methodology for this study, with an outline of both Aeolus and the other observing systems that are used to validate these measurements. Section 3 shows the first example of GWs measured in Aeolus data, and uses other observations and ERA5 reanalysis to validate these results. Section 4 discusses the limitations of the methods used and summarizes the key points from this study.

2. Data and Methods

The purpose of this case study is to determine whether Aeolus is a suitable platform for observing GWs, and to give a first suggestion of the possibilities it presents for wider GW studies. First, a large GW event on July 26, 2019, is established as a good candidate using carefully selected along-track vertical profiles from Aeolus. The data are detrended using a band-pass filter to extract wind perturbations, and the coinciding meteorological and geographical context is assessed to determine if the observed GW structure is plausible.

Validation of this GW event in the Aeolus observations is then carried out using data from the Compact Rayleigh Autonomous Lidar (CORAL) in Tierra del Fuego, the AIRS instrument onboard the Aqua satellite, and output from the ERA5 reanalysis. For a comparison between the two, an Aeolus profile which provides a good demonstration of the broader GW signature is empirically selected, and then co-location profiles from CORAL, AIRS, and ERA5 are found nearby in time and space. Differences between the data sets mean that slightly different procedures are required to extract GW perturbations for each, as described below.

2.1. Aeolus

Aeolus is the first satellite with a space-borne wind lidar instrument onboard (Chanin et al., 1989; ESA, 1989, 2008; Reitebuch, 2012; Stoffelen et al., 2005). This instrument, known as the Atmospheric Laser Doppler Instrument (ALADIN), probes the lowermost 30 km of the atmosphere and provides high vertical resolution profiles of wind, aerosol, and cloud along its orbital path. The satellite has a sun-sychronous orbit with 15.6 orbits per day and a repeat cycle of 7 days. The orbit's inclination is 96.97° and its mean altitude is 320 km, with an ascending-node local equator-crossing time of 18:00. Both the laser and telescope are directed at 35° off-nadir, perpendicular to the direction of travel.

A single wind component v_{LOS} is measured along this line-of-sight (LOS), which is converted into the HLOS wind speed v_{HLOS} by assuming that the vertical wind speed w is small. Equations 1 and 2 show how these parameters relate to the three cartesian wind components u, v and w; where θ is the elevation of the target-to-satellite pointing vector (55°) and Ψ is the bearing of the satellite track.

$$v_{\mathrm{LOS}} = v_{\mathrm{HLOS}} \cos(\theta) + w \sin(\theta) \tag{1}$$

$$v_{\mathrm{HLOS}} = -u \sin(\Psi) - v \cos(\Psi) \tag{2}$$

ALADIN measures backscattering from atmospheric molecules (Rayleigh scattering), and aerosol and hydrometeors (Mie scattering) in the path of the light from its laser, which is operated at a wavelength of 355 nm. The backscattered light is received using a 55 kg telescope which is 1.5 m in diameter, and the Doppler shift of this signal relative to the laser pulse frequency is recorded. These data are processed to produce a measurement of the HLOS wind speed for both the Mie and Rayleigh scattering throughout the depth of the atmospheric profile (Rennie et al., 2020). The vertical domain is split into "range bins" (combined collections of measurements in a given altitude range) which are between 250 and 2,000 m in depth and can be chosen and altered from the ground, with the instrument arranging data into these bins according to the time difference between the laser pulse being transmitted and the return signal being received. In the UTLS region, the vertical resolution of Aeolus wind data is typically ~1 km.

Aeolus data used in this study are aggregated into profiles according to grouping identifiers within each file (De Kloe et al., 2020), with each profile ~87 km apart. The L2B product is used; for this product, each observation is categorized as occurring in either clear or cloudy conditions, and an associated HLOS error estimate is also provided for quality control. Only Rayleigh clear observations are used in this study to maximize data coverage in combination with data quality. An 8 ms^{-1} cut off is used as a filter on the random error for each data point. The data used here has been reprocessed using the baseline B10 of ESA's L2B processor. A number of campaigns have validated the HLOS winds from Aeolus, with the latest estimates for this reprocessed data showing a systematic bias of <1 ms^{-1} for the Rayleigh wind product (Abdalla et al., 2020). Since this study is primarily concerned with wind perturbations, any systematic biases in the data are considered to have a negligible impact on the results.

To plot along-track profiles, the data are linearly interpolated onto a 500 m vertical grid. Wind perturbations are then calculated by running an along-track Savitzky-Golay bandpass filter through the data points, with lower and upper bounds of 7 and 25 profiles, respectively. GWs with along-track horizontal wavelengths of ∼600–2,000 km are detectable using this method. This detrending method is chosen because it best highlights the orientation of the GW for this particular case study. Unlike at higher altitudes, there is no clear scale separation between GWs and other atmospheric features, such as jet streaks, synoptic-scale Rossby waves and various mesoscale phenomena (Perlwitz & Graf, 2001; C. Sun et al., 2014). In this example, the low cutoff point should remove smaller-scale perturbations which might not be related to GW activity, however, caution ought to be applied if using this detrending method in the general case.

2.2. Compact Rayleigh Autonomous Lidar

The CORAL instrument is an autonomous ground-based lidar system designed to provide temperature and density profiles of the middle atmosphere (B. Kaifler & N. Kaifler, 2020). Situated at Tierra del Fuego on the southern tip of South America (54°S, 68°W), it is positioned at a prime location for measuring strong orographic GW activity (N. Kaifler et al., 2020). The altitude range covered by CORAL measurements extends from 15 to 90 km, and measurements have a 900 m vertical resolution oversampled onto a 90 m grid, with a temporal resolution of 20 min. CORAL measures backscattered photons detected in three Rayleigh channels (532 nm) and one Raman channel (608 nm), in clear-sky conditions only. In this study, the Raman channel is used for altitudes below 31 km.

As discussed by Ehard et al. (2015), estimating temperature perturbations using a lidar such as CORAL can be challenging, especially where there are sudden changes in the vertical temperature gradient, such as at the stratopause. Using temporal filtering would alleviate this issue, however, due to the short observational periods on this particular day, such a method is not possible for this case study. Instead, to obtain temperature perturbations a vertical Savitzky-Golay high-pass filter is run with a cut-off wavelength of 20 km. This is in line with previous studies (e.g., B. Kaifler et al., 2015; N. Kaifler et al., 2020) and should be sufficient to observe the important characteristics of this GW.

2.3. Atmospheric Infrared Sounder

The AIRS instrument is a 2378-channel infrared nadir sounder onboard NASA's Aqua satellite (Aumann et al., 2003; Chahine et al., 2006). A part of the A-Train satellite constellation, Aqua is in a sun-synchronous orbit with 14.55 orbits per day, a repeat cycle of 16 days, an orbital inclination of 98.20°, and an ascending-node local equator-crossing time of 13:30. The AIRS instrument scans across track in a ±49.5° wide swath, measuring radiances. The horizontal resolution varies from ∼13.5 × 13.5 km at nadir to 41 × 21.4 km at the track edge, and measurement data are stored in “granules,” each corresponding to 6 min of data (Wright et al., 2017).

In order to provide enough context for the Aeolus overpass, one AIRS granule before and one after the Aeolus overpass are chosen, each with good spatial coverage of the Southern Andes. The retrieval outlined by Hoffmann and Alexander (2009) has been used to estimate air temperature on a 3 km vertical grid from 18–55 km altitude, and results are shown at the 30 km altitude level to avoid vertical edge-truncation effects and as a representative snapshot. Temperature perturbations have been calculated by running a cross-track fourth-order polynomial fit through the data as demonstrated in Alexander and Barnet (2007). GWs with cross-track horizontal wavelengths of ∼50–1,000 km are detectable using this method (e.g., Ern et al., 2016; Hoffmann et al., 2014).

2.4. ERA5

ERA5 is a reanalysis data set provided by the ECMWF which combines an earth-system model with assimilated observations to provide a historical archive of the state of the atmosphere (Hersbach et al., 2020). The data set has a spatial resolution of 0.25° × 0.25° (∼31 km), 137 vertical levels from the surface up to 0.1 hPa, and a temporal resolution of 1 hour. Since Aeolus observations are not assimilated into ERA5, the two data sets are entirely independent of each other. As the Aeolus overpass studied here occurs at almost exactly

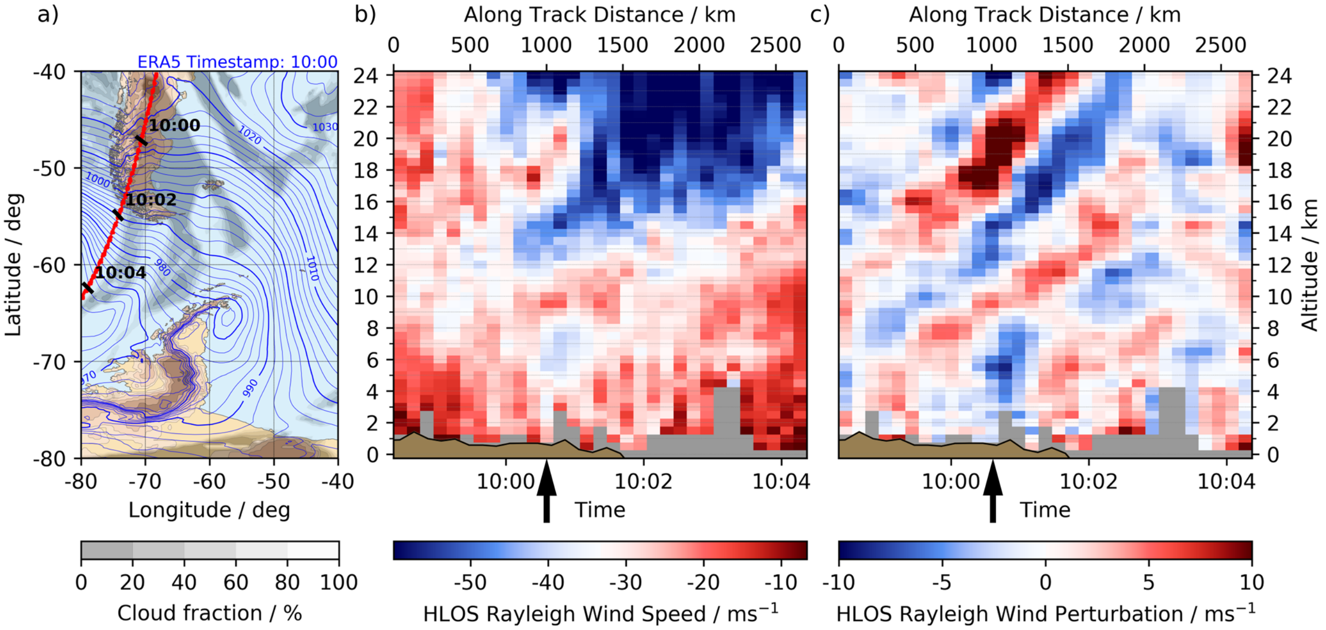

Figure 1. Aeolus overpass of July 26, 2019 with (a) a map showing its geographical context, overlaid with ERA5 data on a single-level for cloud fraction and mean sea-level pressure, and terrain data from the TerrainBase Global Terrain Model; (b) raw winds in an along-track timeseries of the L2B HLOS Rayleigh wind speed product, with color range set by the mean and two standard deviations of the domain; (c) wind perturbations calculated using a 7–25 data point Savitzky-Golay band pass filter. Cloudy or missing data points are obscured with a gray mask. The profile used for the validation of the GW in Aeolus is marked with a black arrow, and corresponds to July 26, 2019, 10:00:34. GW, gravity wave; HLOS, horizontal line-of-sight.

10:00, this is also the time chosen for the ERA5 vertical profile. In order to directly compare the data from the Aeolus overpass with ERA5, the latter is interpolated bi-linearly onto each Aeolus measurement point in space. This is done by projecting the ERA5 u and v wind components onto the Aeolus comparable HLOS, as shown in Equation 2. The data are then further interpolated onto the same 500 m vertical grid as done previously, so that the same horizontal Savitzky-Golay filtering approach can be used. For the multi-data set validation of the GW, the single nearest ERA5 profile to the chosen Aeolus profile is selected rather than interpolating to the measurement location, in order to avoid any aliasing caused by averaging between data points.

Topographical context is provided using 0.25° × 0.25° resolution elevation data from the TBASE archive provided by NCAR, and the elevation for each profile is calculated using a bi-linear interpolation of this data set. The Mean Sea-Level Pressure (MSLP) and cloud fraction layers for the meteorological context are also provided from the hourly ERA5 data at a 0.25° × 0.25° resolution.

3. Results

Figure 1 demonstrates clearly for the first time that GWs can be observed using a space-borne wind lidar. The figure shows winds measured by Aeolus over the Andes on July 26, 2019. The meteorological context is a deep depression, west of the Drake Passage, driving a strong westerly wind over the Southern Andes. This pattern causes significant surface wind stresses which typically translate to strong upward-propagating orographic GWs; such a mechanism is consistent with the characteristics of the observed wave. Aeolus is on the descending node of its orbit, and travels down the length of South America before intersecting the mountain range and heading out over the Pacific Ocean. The cloud fraction overlay from ERA5 shows clear skies along much of the satellite ground-track, providing confidence that it is appropriate to use the Rayleigh-clear HLOS wind product.

The wave can be seen clearly in the HLOS wind field between 10:00 and 10:02 in Figure 1b as absolute measured values, and in Figure 1c as perturbations to the background wind. It coincides geographically with a region of raised topography and appears to be propagating upwards into the stratosphere. At ~15 km altitude and at the time indicated by the black arrow, the GW has a vertical wavelength of ∼8 km, a horizontal wavelength of ∼900 km, and an amplitude of ∼10 m/s; determined empirically because the spacing of the original data makes spectral analysis difficult to implement. Additionally, there is evidence of increasing vertical wavelength with both background wind speed, which increases toward the southern end of the mountains, and altitude. Also of note is the polar night jet, seen in the lower stratosphere poleward of 50°S, and visible as a large region of negative HLOS wind in the upper-right of Figure 1b. The Savitzky-Golay filtering emphasizes the GW in the wind perturbations in Figure 1c, showing diagonally oriented wave fronts which are most pronounced during the same time-frame.

Validation of the GW has been carried out using the CORAL lidar, AIRS, and ERA5 reanalysis, and is shown in Figure 2. Distinct quasi-stationary wave-fronts can be seen in the CORAL lidar timeseries (Figure 2a), with a vertical wavelength of ∼10 km and an amplitude of ∼15 K peaking near the stratopause. The AIRS overpasses before and after the Aeolus pass also show pronounced GW structures emanating eastwards from the Southern Andes (Figures 2b and 2c). The horizontal wavelength in AIRS along the Aeolus track compares well with the 900 km distance observed by Aeolus, lending confidence that they are observing the same wave.

Figure 2d compares a selected profile from the 10 a.m. Aeolus overpass with co-located profiles from each data set, contextualized with the nearest ERA5 profile in both temperature and projected HLOS wind. All measurements are geographically close to the Aeolus profile, except the CORAL lidar which lies 600 km south-east. Note that, according to theory, there is an expected phase difference of 90° between wind and temperature.

Between 5 and 6 a.m., strong temperature perturbations can be seen in CORAL and AIRS, increasing in amplitude with height. The vertical positions of the AIRS temperature peaks match CORAL at 25 and 37 km, but appear to be in anti-phase around 50 km. This is likely due to the poor vertical resolution of AIRS aliasing the wave; this issue is explored further in Section 4. ERA5 at the same time also shows perturbations in temperature and wind, particularly below 20 km in the wind profile. Once again, phase differences with AIRS are likely a result of aliasing, whereas differences with CORAL are more likely to be due to the 600 km distance between the profiles.

At 10 a.m., there is good agreement between the Aeolus and ERA5 winds, particularly in amplitude, although with a slight vertical phase offset increasing gradually with height. Large temperature perturbations in the CORAL profile confirm the expectation of strong GW activity coinciding with the Aeolus overpass. The relative amplitude change at each height between 5–6 a.m. and 10 a.m. is consistent with ERA5. The reanalysis however does not quite capture the amplitude that CORAL does, which could be due to the wave dissipating too quickly in the reanalysis, the stratopause interfering with the filtering process for CORAL or the difference in sampling location between the two profiles. Also of note is a sudden reduction in the ERA5 amplitude above 45 km, likely explained by the sponge layer kicking in at this height.

At 7 p.m., only the AIRS observations are available for comparison, and this profile shows the wave structure from 5 to 6 a.m. largely persisting through the day until 7 p.m. It is difficult to compare this with ERA5 due to significant deficiencies in both data sets, especially at higher altitudes; however, it is important to note that a large GW is seen in both profiles. Throughout the measurement period, the AIRS-derived amplitude is significantly larger than that in the other data sets. The reasons for this are unclear, but may involve inaccurate model physics, the choice of detrending approach, or the different location from the CORAL lidar.

Figure 3 shows ERA5 data projected onto the HLOS wind points observed by Aeolus. The middle and right panels show striking morphological agreement with Figures 1b and 1c. As in the observations, a strong orographic GW is seen propagating upwards into the stratosphere above the sharp Andean topography. The vertical wavelength is of similar magnitude to that seen in Aeolus, although, importantly, not as high. This suggests that the model may underestimate the amplitude of such waves as well as exhibit the phase differences described above.

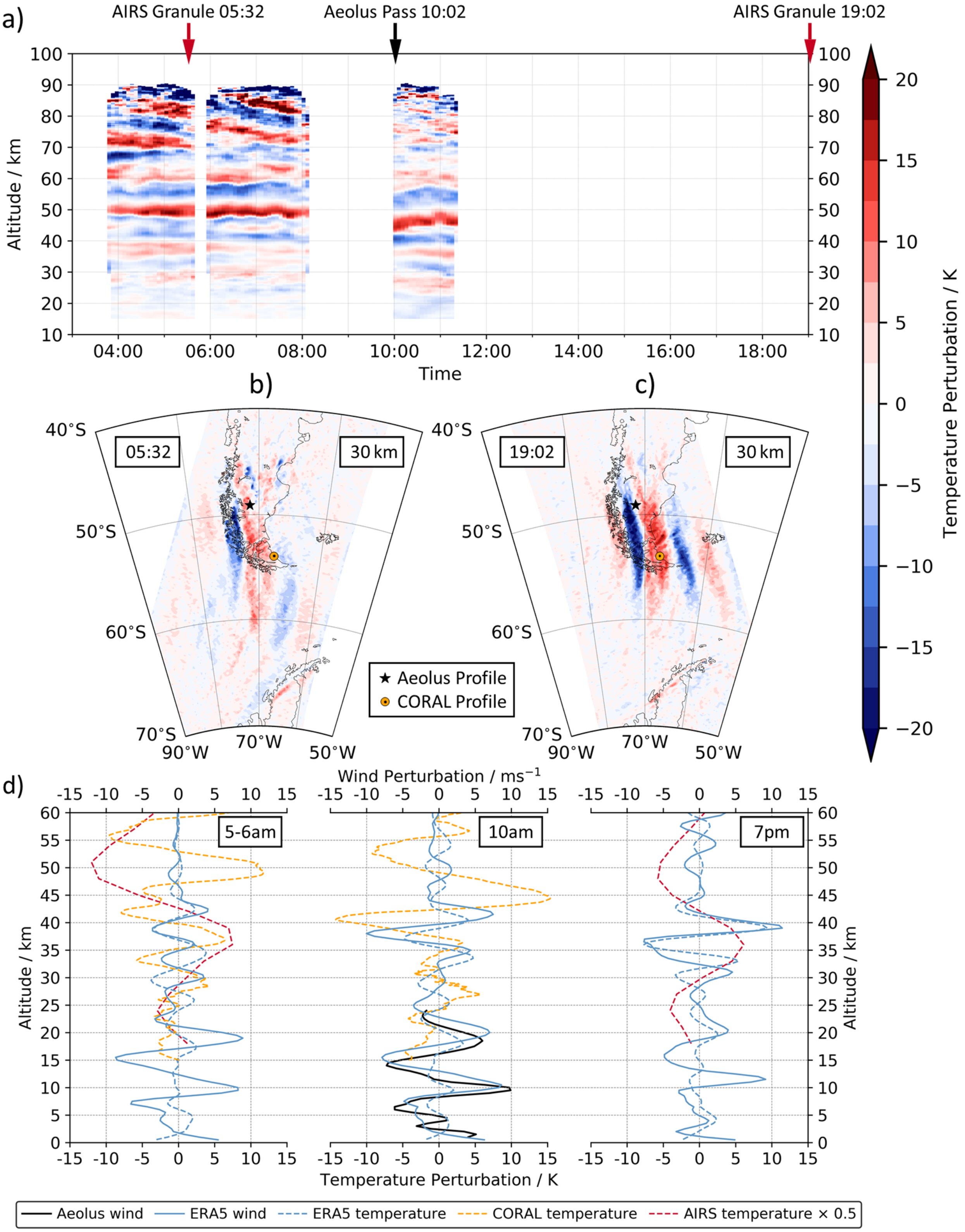

Figure 2. (a) Timeseries of kinetic temperature perturbations from the CORAL lidar at Tierra del Fuego for July 26, 2019 at 15-min resolution. (b and c) Data granules 55 and 190 from the AIRS instrument for 05:32 and 19:02 respectively and at an altitude of 30 km. (d) Three time snapshots comparing data from Aeolus with CORAL and AIRS observations and ERA5 reanalysis. AIRS has been multiplied by 0.5 for ease of comparison. AIRS, Atmospheric Infrared Sounder.

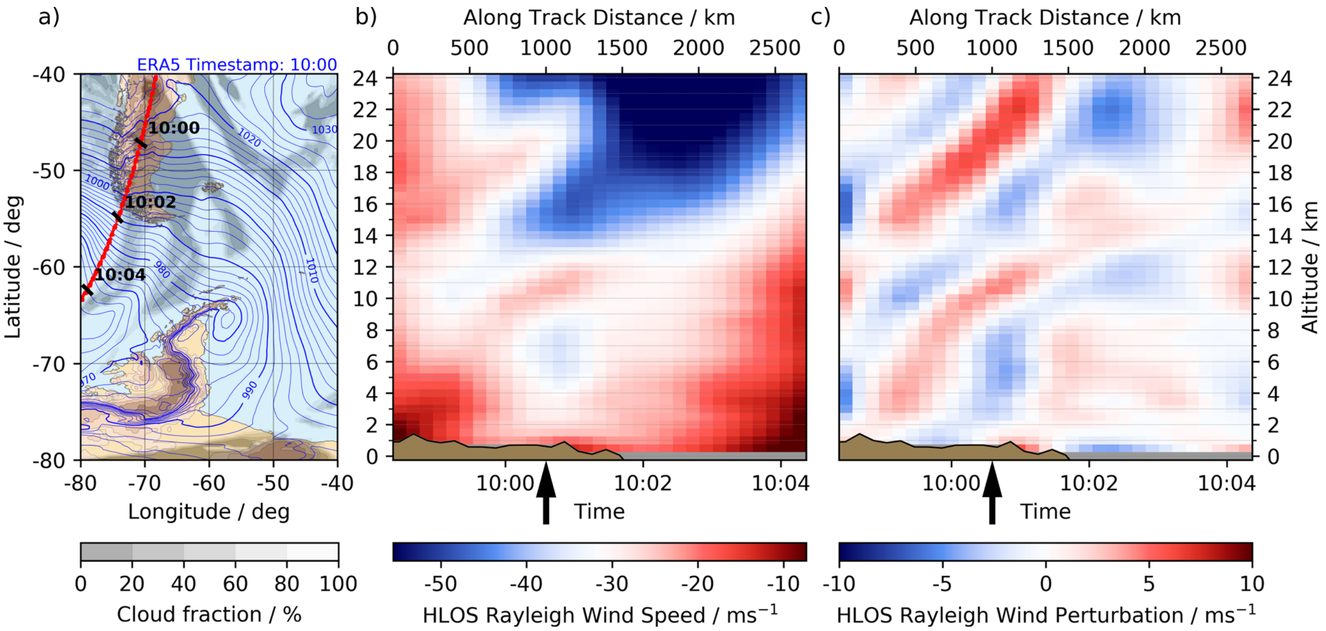

Figure 3. ERA5 validation of the Aeolus overpass of July 26, 2019 with (a) a map showing its geographical context, overlaid with ERA5 data on a single-level for cloud fraction and mean sea-level pressure, and terrain data from the TerrainBase Global Terrain Model; (b) ERA5 HLOS projected winds to match with the Aeolus along-track profile, with color range set by the mean and two standard deviations of the domain; (c) wind perturbations calculated using a 7–25 data point Savitzky-Golay band pass filter. Cloudy or missing data points are obscured with a gray mask. The profile used for the validation of the GW in Aeolus is marked with a black arrow, and corresponds to July 26, 2019, 10:00:34. GW, gravity wave; HLOS, horizontal line-of-sight.

4. Discussion and Conclusions

The primary limitation for measuring GWs using Aeolus is the complex dynamics of the troposphere and the challenges this presents when detrending the observed data to identify wave perturbations. Unlike in the stratosphere and above, where there is a clear spectral separation between GW perturbations and larger-scale processes, in the troposphere many meteorological processes interfere with the analysis. While this problem is addressed here by empirically selecting a filter which highlights the wave of interest, in the general case this is a larger technical challenge, and will require significant research before these results can be generalized (e.g., Rapp et al., 2018).

Furthermore, Aeolus only measures in one wind direction and only provides data along its flight track. Thus, no information about the orientation or true horizontal wavelength of the measured GWs can be inferred. Instead, only the projection of the horizontal wavelength along the satellite track can be determined, which overestimates the true horizontal wavelength. For orographic GWs over the Andes, this strongly restricts the information Aeolus can provide about horizontal structure, especially when the satellite bearing is near-parallel to the mountain range as in this study.

Additionally, the HLOS wind calculation of the Aeolus L2B processor assumes zero vertical wind. This is unproblematic under normal conditions; however, where there is strong GW activity, this assumption is less justified due to the strong vertical motions that can be present. For the GW presented in this paper, the error in the HLOS wind is determined to be below 2%; a figure that can be calculated using the gravity wave polarization relations (Fritts & Alexander, 2003). Further, the orientation of the HLOS winds is not near-zonal close to the pole, leading to a strong bias of the measured waves with respect to latitude. This again may add additional technical difficulties for any global studies of GW activities using data from Aeolus.

Finally, there remain general problems of filtering for and spectrally analyzing GWs in observational data, problems that are extensively discussed by, for example, Preusse et al. (2008), Wright, Hindley, Moss, and Mitchell (2016), Strube et al. (2020), and Krisch et al. (2020), among others. The data here have been interpolated onto a regular grid in order to carry out the Savitzky-Golay filtering, a process which itself will tend to smooth the peaks of each wave and reduce their amplitude. Furthermore, the transmission of the filter used is inherently imperfect within the wavelength window analyzed; this is a general problem for spectral analysis, but one which adds to the uncertainties in such work. Here, as in Hindley et al. (2015), the Savitzky-Golay filter is selected as a trade-off between a desirably sharp transition at each end and Gibbs ringing at the discontinuity, but it will be important to assess how well alternative filters perform in more general future work.

Nonetheless, the strong morphological and quantitative agreement in wave properties between the HLOS wind profiles from Aeolus and the temperature-based profiles from CORAL and AIRS leads to a high level of confidence in Aeolus' ability to observe GWs. A clear phase structure is visible from near the surface up to the stratosphere, with the CORAL lidar supplementing this higher up and AIRS providing information about its geographical orientation. Good qualitative agreement is found between these wind and temperature measurements, suggesting that a good phase relationship is observed, even if there is sometimes a phase offset from one location to the next. These results demonstrate the benefit of these spaceborne wind lidar measurements for GW studies, which can be used to better constrain GW parametrizations in models and improve the current understanding of small-scale GW processes.

Data Availability Statement

Aeolus data were provided by the European Space Agency, and can be accessed via https://aeolus-ds.eo.esa.int/oads/access/. The AIRS data were provided by NASA; L1 radiance data can be acquired via https://disc.gsfc.nasa.gov/, and were retrieved to L2 temperatures using the method described by Hoffmann and Alexander (2009). ERA5 data can be accessed from the Copernicus Climate Data Store, https://cds.climate.copernicus.eu/. CORAL Lidar data used for this study have been archived at https://halo-db.pa.op.dlr.de/dataset/7620

Acknowledgments
The authors would like to thank the Aeolus DISC team for supporting this study and for their helpful communications throughout. The authors also wish to thank two anonymous reviewers for their useful comments on the original manuscript. T. P. Banyard is funded by Royal Society grant RGF/EA/180217 and EPSRC grant EP/R513155/1. C. J. Wright is funded by Royal Society grant UF160545 and NERC grant NE/S00985X/1. C. J. Wright and N. P. Hindley are funded by NERC grant NE/R001391/1. Open Access funding enabled and organized by Projekt DEAL.

References

Abdalla, S., Aprile, S., Mellano, L., De Laurentis, M., Fischer, P., Von Bismarck, J., & Isaksen, L. (2020). *Aeolus: First FM-B science data reprocessing campaign*. Aeolus CAL/VAL and Science Workshop 2020.

Alexander, M. J. (1998). Interpretations of observed climatological patterns in stratospheric gravity wave variance. *Journal of Geophysical Research*, *103*(D8), 8627–8640. https://doi.org/10.1029/97JD03325

Alexander, M. J., & Barnet, C. (2007). Using satellite observations to constrain parameterizations of gravity wave effects for global models. *Journal of the Atmospheric Sciences*, *64*(5), 1652–1665. https://doi.org/10.1175/JAS3897.1

Alexander, M. J., Geller, M., McLandress, C., Polavarapu, S., Preusse, P., Sassi, F., et al. (2010). Recent developments in gravity-wave effects in climate models and the global distribution of gravity-wave momentum flux from observations and models. *Quarterly Journal of the Royal Meteorological Society*, *136*(650), 1103–1124. https://doi.org/10.1002/qj.637

Alexander, M. J., & Teitelbaum, H. (2011). Three-dimensional properties of Andes mountain waves observed by satellite: A case study. *Journal of Geophysical Research*, *116*(D23). https://doi.org/10.1029/2011JD016151

Aumann, H. H., Chahine, M. T., Gautier, C., Goldberg, M. D., Kalnay, E., McMillin, L. M., et al. (2003). AIRS/AMSU/HSB on the Aqua mission: Design, science objectives, data products, and processing systems. *IEEE Transactions on Geoscience and Remote Sensing*, *41*(2), 253–264. https://doi.org/10.1109/TGRS.2002.808356

Bramberger, M., Dörnbrack, A., Wilms, H., Gemsa, S., Raynor, K., & Sharman, R. (2018). Vertically propagating mountain waves-A hazard for high-flying aircraft? *Journal of Applied Meteorology and Climatology*, *57*(9), 1957–1975. https://doi.org/10.1175/JAMC-D-17-0340.1

Chahine, M. T., Pagano, T. S., Aumann, H. H., Atlas, R., Barnet, C., Blaisdell, J., et al. (2006). AIRS. *Bulletin of the American Meteorological Society*, *87*(7), 911–926. https://doi.org/10.1175/BAMS-87-7-911

Chanin, M. L., Garnier, A., Hauchecorne, A., & Porteneuve, J. (1989). A Doppler lidar for measuring winds in the middle atmosphere. *Geophysical Research Letters*, *16*(11), 1273–1276. https://doi.org/10.1029/GL016i011p01273

De Kloe, J., Stoffelen, A., Tan, D., Andersson, E., Rennie, M., Dabas, A., et al. (2020). *ADM-aeolus level-2B/2C processor input/output data definitions interface control document* (p. 110). ESA.

Dunkerton, T. J. (1997). The role of gravity waves in the quasi-biennial oscillation. *Journal of Geophysical Research*, *102*(D22), 26053–26076. https://doi.org/10.1029/96JD02999

Ehard, B., Kaifler, B., Dörnbrack, A., Preusse, P., Eckermann, S. D., Bramberger, M., et al. (2017). Horizontal propagation of large-amplitude mountain waves into the polar night jet. *Journal of Geophysical Research: Atmospheres*, *122*(3), 1423–1436. https://doi.org/10.1002/2016JD025621

Ehard, B., Kaifler, B., Kaifler, N., & Rapp, M. (2015). Evaluation of methods for gravity wave extraction from middle-atmospheric lidar temperature measurements. *Atmospheric Measurement Techniques*, *8*, 4645–4655. https://doi.org/10.5194/amt-8-4645-2015

Eichinger, R., Garny, H., Šácha, P., Danker, J., Dietmüller, S., & Oberländer-Hayn, S. (2020). Effects of missing gravity waves on stratospheric dynamics; part 1: Climatology. *Climate Dynamics*, *54*(5), 3165–3183. https://doi.org/10.1007/s00382-020-05166-w

Ern, M., Hoffmann, L., & Preusse, P. (2016). Directional gravity wave momentum fluxes in the stratosphere derived from high-resolution AIRS temperature data. *Geophysical Research Letters*, *44*(1), 475–485. https://doi.org/10.1002/2016GL072007

Ern, M., Ploeger, F., Preusse, P., Gille, J. C., Gray, L. J., Kalisch, S., et al. (2014). Interaction of gravity waves with the QBO: A satellite perspective. *Journal of Geophysical Research: Atmospheres*, *119*(5), 2329–2355. https://doi.org/10.1002/2013JD020731

Ern, M., Preusse, P., Alexander, M., & Warner, C. (2004). Absolute values of gravity wave momentum flux derived from satellite data. *Journal of Geophysical Research*, *109*(D20). https://doi.org/10.1029/2004JD004752

ESA. (1989). *ALADIN—Atmospheric Laser Doppler Instrument* (Working Group Report ESA SP-1112).

ESA. (2008). *ADM-Aeolus Science Report* (ESA SP-1311).

Fritts, D. C. (1984). Gravity wave saturation in the middle atmosphere: A review of theory and observations. *Reviews of Geophysics*, *22*(3), 275–308. https://doi.org/10.1029/RG022i003p00275

Fritts, D. C., & Alexander, M. (2003). Gravity wave dynamics and effects in the middle atmosphere. *Reviews of Geophysics*, *41*(1). https://doi.org/10.1029/2001RG000106

Geller, M. A., Alexander, M. J., Love, P. T., Bacmeister, J., Ern, M., Hertzog, A., et al. (2013). A comparison between gravity wave momentum fluxes in observations and climate models. *Journal of Climate*, *26*(17), 6383–6405. https://doi.org/10.1175/JCLI-D-12-00545.1

Hersbach, H., Bell, B., Berrisford, P., Hirahara, S., Horányi, A., Muñoz-Sabater, J., et al. (2020). The ERA5 global reanalysis. *Quarterly Journal of the Royal Meteorological Society*, *146*(730), 1999–2049. https://doi.org/10.1002/qj.3803

Hindley, N. P., Wright, C. J., Smith, N. D., & Mitchell, N. J. (2015). The southern stratospheric gravity wave hot spot: Individual waves and their momentum fluxes measured by COSMIC GPS-RO. *Atmospheric Chemistry and Physics*, *15*(14), 7797–7818. https://doi.org/10.5194/acp-15-7797-2015

Hines, C. O. (1960). Internal atmospheric gravity waves at ionospheric heights. *Canadian Journal of Physics*, *38*(11), 1441–1481. https://doi.org/10.1139/p60-150

Hoffmann, L., & Alexander, M. J. (2009). Retrieval of stratospheric temperatures from Atmospheric Infrared Sounder radiance measurements for gravity wave studies. *Journal of Geophysical Research*, *114*(D7). https://doi.org/10.1029/2008JD011241

Hoffmann, L., Alexander, M. J., Clerbaux, C., Grimsdell, A. W., Meyer, C. I., Rößler, T., & Tournier, B. (2014). Intercomparison of stratospheric gravity wave observations with AIRS and IASI. *Atmospheric Measurement Techniques*, *7*, 4517–4537. https://doi.org/10.5194/amt-7-4517-2014

Hoffmann, L., Xue, X., & Alexander, M. J. (2013). A global view of stratospheric gravity wave hotspots located with Atmospheric Infrared Sounder observations. *Journal of Geophysical Research: Atmospheres*, *118*(2), 416–434. https://doi.org/10.1029/2012jd018658

Holton, J. R. (1983). The influence of gravity wave breaking on the general circulation of the middle atmosphere. *Journal of the Atmospheric Sciences*, *40*(10), 2497–2507. https://doi.org/10.1175/1520-0469(1983)040<2497:TIOGWB>2.0.CO;2

Jiang, J. H., Wu, D., & Eckermann, S. (2002). Upper Atmosphere Research Satellite (UARS) MLS observation of mountain waves over the Andes. *Journal of Geophysical Research*, *107*(D20), SOL-15. https://doi.org/10.1029/2002JD002091

Jones, P. W., Hamilton, K., & Wilson, R. J. (1997). A very high resolution general circulation model simulation of the global circulation in austral winter. *Journal of the Atmospheric Sciences*, *54*(8), 1107–1116. https://doi.org/10.1175/1520-0469(1997)054<1107:AVHRGC>2.0.CO;2

Kaifler, B., & Kaifler, N. (2020). A Compact Rayleigh Autonomous Lidar (CORAL) for the middle atmosphere. *Atmospheric Measurement Techniques*, 1–24. https://doi.org/10.5194/amt-2020-418

Kaifler, B., Lübken, F.-J., Höffner, J., Morris, R. J., & Viehl, T. P. (2015). Lidar observations of gravity wave activity in the middle atmosphere over Davis (69°S, 78°E), Antarctica. *Journal of Geophysical Research: Atmospheres*, *120*(10), 4506–4521. https://doi.org/10.1002/2014JD022879

Kaifler, N., Kaifler, B., Dörnbrack, A., Rapp, M., Hormaechea, J. L., & de la Torre, A. (2020). Lidar observations of large-amplitude mountain waves in the stratosphere above Tierra del Fuego, Argentina. *Scientific Reports*, *10*, 1–10. https://doi.org/10.1038/s41598-020-71443-7

Kim, Y., Eckermann, S., & Chun, H. (2003). An overview of the past, present and future of gravity-wave drag parametrization for numerical climate and weather prediction models. *Atmosphere-Ocean*, *41*(1), 65–98. https://doi.org/10.3137/ao.410105

Krisch, I., Ern, M., Hoffmann, L., Preusse, P., Strube, C., Ungermann, J., et al. (2020). Superposition of gravity waves with different propagation characteristics observed by airborne and space-borne infrared sounders. *Atmospheric Chemistry and Physics*, *20*(19), 11469–11490. https://doi.org/10.5194/acp-20-11469-2020

Krisch, I., Preusse, P., Ungermann, J., Dörnbrack, A., Eckermann, S. D., Ern, M., et al. (2017). First tomographic observations of gravity waves by the infrared limb imager GLORIA. *Atmospheric Chemistry and Physics*, *17*(24), 14937–14953. https://doi.org/10.5194/acp-17-14937-2017

Larsen, M., Kelley, M., & Gage, K. (1982). Turbulence spectra in the upper troposphere and lower stratosphere at periods between 2 hours and 40 days. *Journal of the Atmospheric Sciences*, *39*(5), 1035–1041. https://doi.org/10.1175/1520-0469(1982)039<1035:TSITUT>2.0.CO;2

Lilly, D. K. (1978). A severe downslope windstorm and aircraft turbulence event induced by a mountain wave. *Journal of the Atmospheric Sciences*, *35*(1), 59–77. https://doi.org/10.1175/1520-0469(1978)035<0059:ASDWAA>2.0.CO;2

McFarlane, N. A. (1987). The effect of orographically excited gravity wave drag on the general circulation of the lower stratosphere and troposphere. *Journal of the Atmospheric Sciences*, *44*(14), 1775–1800. https://doi.org/10.1175/1520-0469(1987)044<1775:TEOOEG>3E2.0.CO;2

Palmer, T. N., Shutts, G. J., & Swinbank, R. (1986). Alleviation of a systematic westerly bias in general circulation and numerical weather prediction models through an orographic gravity wave drag parametrization. *Quarterly Journal of the Royal Meteorological Society*, *112*(474), 1001–1039. https://doi.org/10.1002/qj.49711247406

Perlwitz, J., & Graf, H.-F. (2001). The variability of the horizontal circulation in the troposphere and stratosphere - a comparison. *Theoretical and Applied Climatology*, *69*(3–4), 149–161. https://doi.org/10.1007/s007040170021

Preusse, P., Eckermann, S. D., & Ern, M. (2008). Transparency of the atmosphere to short horizontal wavelength gravity waves. *Journal of Geophysical Research*, *113*(D24). https://doi.org/10.1029/2007JD009682

Rapp, M., Dörnbrack, A., & Preusse, P. (2018). Large midlatitude stratospheric temperature variability caused by inertial instability: A potential source of bias for gravity wave climatologies. *Geophysical Research Letters*, *45*(19), 682–10. https://doi.org/10.1029/2018GL079142

Reitebuch, O. (2012). The spaceborne wind lidar mission ADM-Aeolus. *Atmospheric Physics*, 815–827. https://doi.org/10.1007/978-3-642-30183-4_49

Rennie, M., Tan, D., Andersson, E., Poli, P., Dabas, A., De Kloe, J., et al. (2020). *Aeolus level-2B algorithm theoretical basis document (mathematical description of the aeolus L2B processor)*. ESA.

Sato, K., Tateno, S., Watanabe, S., & Kawatani, Y. (2012). Gravity wave characteristics in the southern hemisphere revealed by a high-resolution middle-atmosphere general circulation model. *Journal of the Atmospheric Sciences*, *69*(4), 1378–1396. https://doi.org/10.1175/JAS-D-11-0101.1

Siskind, D. E., Eckermann, S. D., Coy, L., McCormack, J. P., & Randall, C. E. (2007). On recent interannual variability of the Arctic winter mesosphere: Implications for tracer descent. *Geophysical Research Letters*, *34*(9). https://doi.org/10.1029/2007GL029293

Stoffelen, A., Pailleux, J., Källén, E., Vaughan, J. M., Isaksen, L., Flamant, P., et al. (2005). The atmospheric dynamics mission for global wind field measurement. *Bulletin of the American Meteorological Society*, *86*(1), 73–88. https://doi.org/10.1175/BAMS-86-1-73

Strube, C., Ern, M., Preusse, P., & Riese, M. (2020). Removing spurious inertial instability signals from gravity wave temperature perturbations using spectral filtering methods. *Atmospheric Measurement Techniques*, *13*(9), 4927–4945. https://doi.org/10.5194/amt-13-4927-2020

Sun, B., Reale, A., Seidel, D. J., & Hunt, D. C. (2010). Comparing radiosonde and COSMIC atmospheric profile data to quantify differences among radiosonde types and the effects of imperfect collocation on comparison statistics. *Journal of Geophysical Research*, *115*(D23). https://doi.org/10.1029/2010JD014457

Sun, C., Li, J., Jin, F.-F., & Xie, F. (2014). Contrasting meridional structures of stratospheric and tropospheric planetary wave variability in the northern hemisphere. *Tellus A: Dynamic Meteorology and Oceanography*, *66*(1), 25303. https://doi.org/10.3402/tellusa.v66.25303

Vincent, R. A., & Reid, I. M. (1983). HF Doppler measurements of mesospheric gravity wave momentum fluxes. *Journal of the Atmospheric Sciences*, *40*(5), 1321–1333. https://doi.org/10.1175/1520-0469(1983)040<1321:HDMOMG>2.0.CO;2

Watanabe, S., Sato, K., Kawatani, Y., & Takahashi, M. (2015). Vertical resolution dependence of gravity wave momentum flux simulated by an atmospheric general circulation model. *Geoscientific Model Development*, *8*(6), 1637–1644. https://doi.org/10.5194/gmd-8-1637-2015

Wright, C. J., Hindley, N. P., Hoffmann, L., Alexander, M. J., & Mitchell, N. J. (2017). Exploring gravity wave characteristics in 3-D using a novel S-transform technique: AIRS/Aqua measurements over the Southern Andes and Drake Passage. *Atmospheric Chemistry and Physics*, *17*(13), 8553–8575. https://doi.org/10.5194/acp-17-8553-2017

Wright, C. J., Hindley, N. P., & Mitchell, N. J. (2016). Combining AIRS and MLS observations for three-dimensional gravity wave measurement. *Geophysical Research Letters*, *43*(2), 884–893. https://doi.org/10.1002/2015GL067233

Wright, C. J., Hindley, N. P., Moss, A. C., & Mitchell, N. J. (2016). Multi-instrument gravity-wave measurements over Tierra del Fuego and the Drake Passage - Part 1: Potential energies and vertical wavelengths from AIRS, COSMIC, HIRDLS, MLS-Aura, SAAMER, SABER and radiosondes. *Atmospheric Measurement Techniques*, *9*(7), 877–908. https://doi.org/10.5194/amt-9-877-2016

Wright, C. J., Osprey, S. M., Barnett, J. J., Gray, L. J., & Gille, J. C. (2010). High Resolution Dynamics Limb Sounder measurements of gravity wave activity in the 2006 Arctic stratosphere. *Journal of Geophysical Research*, *115*(D2). https://doi.org/10.1029/2009JD011858